Novel detection of dark oxygen production at the abyssal seafloor

Andrew K. Sweetman[1*], Alycia J. Smith[2], Danielle S.W. de Jonge[1], Tobias Hahn[3], Peter Schroedl[4], Michael Silverstein[5], Claire Andrade[4], R. Lawrence Edwards[6], Alastair J.M. Lough[7], Clare Woulds[7], William B. Homoky[7], Andrea Koschinsky[8], Sebastian Fuchs[9], Thomas Kuhn[9], Franz Geiger[10], Jeffrey J. Marlow[4]

[1]The Scottish Association for Marine Science, (SAMS), Oban, UK
[2]Heriot-Watt University, Edinburgh, UK
[3]GEOMAR Helmholtz Centre for Ocean Research Kiel, Kiel, Germany
[4]Department of Biology, Boston University, Boston, Massachusetts, USA
[5]Bioinformatics Program, Boston University, Boston, Massachusetts, USA
[6]Department of Earth and Environmental Science, University of Minnesota, Minneapolis, USA
[7]Faculty of Environment, University of Leeds, Leeds, UK
[8]School of Science (Physics & Earth Sciences), Constructor University Bremen, Germany,
[9]Federal Institute for Geoscience and Natural Resources (BGR), Hannover, Germany
[10]Technological Institute, North-western University, Evanston, Illinois, USA

*Corresponding author email: Andrew.Sweetman@sams.ac.uk

Abstract

***In-situ* O_2 consumption measurements at the polymetallic nodule covered abyssal seafloor revealed O_2 rising to more than three times the background concentration over the course of two days in 95% of experiments. Dark oxygen production (DOP) was detected at multiple sites across the Pacific and was observed in *ex-situ* incubations including in the presence of only nodules. Based on electrochemistry analysis that indicated high voltage potentials (up to 0.95V) on the nodule surfaces, we hypothesise that seawater electrolysis plays a role in DOP, and DOP contributes to biogeochemical cycles and ecological dynamics in polymetallic nodule-bearing environments.**

Main text

Oxygen (O_2) is the most energetically favourable electron acceptor for organic carbon (C_{org}) remineralization and is prevalent in deep-sea surface sediments[1]. All O_2 consumed at the deep-sea floor is thought to originate from photosynthesis and enters the deep ocean via subduction and circulation of waters that were once equilibrated with the atmosphere[2-3]. Seafloor O_2 consumption rates reflect the sum of aerobic respiration as well as biotic and abiotic oxidation of reduced inorganic compounds produced by anaerobic respiration of C_{org}. Collectively, these processes define sediment community O_2 consumption (SCOC)[1,4,5] and quantifying its value is needed to quantify fluxes of major elemental cycles through marine systems and benthic ecosystem functioning. SCOC is measured by observing temporal or spatial changes in O_2 concentration with benthic chambers (BC), sediment O_2 microprofiles or non-invasive eddy correlation. Here, we present data from 41 *in-situ* lander mounted BC experiments deployed to measure abyssal SCOC in the NORI-D licence area of the eastern Clarion-Clipperton Zone (CCZ, Extended Data Fig. 1 and Table 1) where polymetallic nodules cover extensive areas of ocean floor, and we show that more O_2 was accumulating in the chambers than was being consumed resulting in net oxygen production.

Constant linear decreases in O_2 optode readings were observed in some BC experiments (e.g., AKS318-Ch.1 and AKS321-Ch.1, Fig. 1) indicating that SCOC occurs in NORI-D as it does in many other abyssal habitats[4-6]. However, O_2 concentrations in 25 seafloor incubations started at 185.2 ± 2.9 μmol L^{-1} (1 Standard Error [SE]) and reached O_2 maxima between 201 and 819 μmol L^{-1} over 47 hours (Fig. 1). Dark O_2 production (DOP) was non-linear in nature (Fig. 1) and peak O_2 concentrations corresponded to increases of 5 - 335 % above background concentrations indicative of net O_2 production. An independent measure of O_2 concentration using the Winkler method showed DOP in 18 *in-situ* BC experiments that used optodes, as well as 14 *in-situ* BC experiments that did not (Extended data Fig. 2), verifying the DOP and providing evidence that the DOP recorded by the optodes was not the result of malfunctioning sensors. Our findings stand in stark contrast to all previously published deep seafloor O_2 flux studies that have been conducted that only report net O_2 consumption, and suggests DOP may provide O_2 to benthic ecosystems in NORI-D.

The non-linear nature of the O_2 production prevented DOP flux calculations. However, no significant difference in the total O_2 produced (maximum [O_2] – initial [O_2], Extended Date Table 2) was found between chambers (ANOVA, $f_{2,8} = 0.101$, $p = 0.905$, see Online methods), experimental treatments (ANOVA, $f_{3,8} = 0.902$, $p = 0.482$, see Online methods), nor any interaction effects (ANOVA, $f_{1,8} = 0.078$, $p = 0.788$) which rules out experimental biases. No significant difference in the total amount of O_2 produced was found between cruises (ANOVA, $f_{2,12} = 0.391$, $p = 0.684$), but it was significantly correlated to the average surface area of the nodules (Spearman's correlation, $\rho = 0.664$, p=0.031). A re-evaluation of O_2 optode data collected in 2015 and 2018 from 36-hour *in-situ* BC experiments in the abyssal eastern (UK1 and OMS) and western CCZ (Extended Data Fig. 3) showed similar O_2 optode profiles to the DOP profiles in Fig. 1 suggesting DOP maybe widespread across the CCZ.

Several lines of evidence indicate that the DOP was not caused by experimental artefacts. Firstly, we found no significant difference in the total O_2 change between experimental treatments and the no-injection controls (see Online methods) demonstrating that DOP wasn't attributable to the injection of exogenous fluids. The steady increase in O_2 concentration recorded during the incubations over many hours are also inconsistent with a pulsed injection of O_2. Secondly, diffusion of O_2 from trapped air bubbles within the chamber were reasoned to be insignificant because each chamber uses two one-way valves in the lid to purge air from the chambers during deployment, and more than 200 cubic metres of water would have passed through each chamber during the approximately 80-minute descent to the seafloor. Even if an air bubble could be trapped long enough to reach the seafloor, gaseous diffusion of O_2 into the water phase would take < 1 second at most at 4 km depth (Extended data Table 3). By contrast, O_2 concentrations in the well-mixed water phase of the chambers increased steadily over many hours (Fig. 1). Thirdly, we considered diffusion of O_2 from the plastic chamber walls and lid into the water phase and found this to be unlikely also (see Online methods) as the chambers are built from polyoxymethylene, which is both highly inert and chemically stable in well-oxygenated settings. In addition, this scenario would not explain the wide variation in DOP we observed (Fig. 1) since all experiments used identical materials. Lastly, *ex-situ* DOP was observed during 48-hour sediment core incubations carried out on the ship in the dark at *in-situ* temperature during the 5D expedition (Extended data Fig. 4). Thus, all our evidence indicates that DOP was occurring at the seafloor.

Several lines of inquiry were pursued to provide an explanation for the observation of seafloor DOP. Sub-surface advection of oxic-bottom water from seamounts into sediments (as observed along seamount flanks)[7,8] and the subsequent diffusion of oxygenated porewaters into the chambers was discounted as the cause for the DOP based on *in-situ* O_2 microprofiling, which showed that porewater was a net sink for O_2 and was undersaturated compared to the incubation chambers. Furthermore, DOP was measured in sealed *ex-situ* experiments (Extended data Fig. 4) that prevented O_2 intrusion from below.

Recent detections of oxygen-producing metabolisms[9] and aphotic ecosystems[10] suggest that much remains to be discovered with regard to biological oxygenic activity, particularly in association with nitrogen cycling. It is unlikely that biological mechanisms were responsible for the bulk of the DOP as *ex-situ* core incubations revealed DOP in the presence of mercury chloride ($HgCl_2$) (Extended data Figure 4). While many microbes in the CCZ are able to detoxify Hg (II) to Hg (0)[11], those taxa capable of DOP (e.g., *Nitrosopumilus maritimus*) are known to be killed by its addition[9]. Furthermore, we observed weak statistical support between the relative abundance of certain nitrogen-cycling microbial taxa and DOP (e.g., *Nitrospira* $\rho = 0.791$, $p = 0.111$; *Candidatus Nitrosopumilus* $\rho = 0.474$, $p = 0.420$), which collectively suggested that microbial activity unlikely accounted for the bulk of measured DOP.

The fact that DOP was detected in *ex-situ* controls containing only polymetallic nodules (i.e., no sediment, Extended data Fig. 4) suggest that the DOP was linked to presence of the nodules. Polymetallic nodules can be radioactive[12] and the radiolysis of water via the decay chains of ^{40}K, ^{232}Th, ^{235}U, and ^{238}U in deep-sea sediments can generate molecular hydrogen[13-14], as well as hydrogen peroxide (H_2O_2)[15] and a range of other reactive oxygen species[16] that can lead to the production of O_2[17]. We estimated the potential contribution of radiolytic O_2 production from the overlying water, nodules, and sediment, and scaled this value by the benthic chamber's size to calculate that 0.18 μmol L^{-1} O_2 would be generated in the chambers in 48 hours. Chemical reduction of solid manganese (IV) oxide (birnessite) to dissolved manganese (II) can lead to the liberation of O_2 ($2MnO_2 \rightarrow 2MnO + O_2$), and this reaction accelerates as both the ambient O_2 concentration and pH decrease (Extended data Fig. 5). We modelled the chemical reduction of manganese (IV) oxide at *in-situ* temperature (1.6°C) across a range of pH and O_2 conditions encountered at the seafloor and found that <0.1 nmol of manganese (IV) oxide would be chemically reduced to manganese (II) (Extended data Fig. 5). As such, localized radiolytic O_2 production from the sediments and nodules, and chemical dissolution explains only a negligible proportion (< 0.5 %) of the DOP observed.

The oxygen evolution reaction (OER) in seawater requires an input voltage of 0.8 V plus an overpotential of approx. 0.37 V to split seawater into H_2 and O_2[18] at the mean pH at the seafloor in NORI-D (7.41). This value can be lowered by several hundred millivolts if the reaction proceeds through the lattice-oxygen-mediated mechanism[19]. The use of metal catalysts such as Mn- and Fe-oxides enriched with transition metals (e.g., Ni, Co, or Cu) that are found in nodules[20] can also lower the voltage needed for H_2 and O_2 generation, increase electrical conductivity, and optimize the adsorption of reactants and intermediates[21,22]. We tested the electrical potential between two platinum electrodes at 165 sites on the surfaces of 12 nodules from the UK1, NORI-D, and BGR license areas that had been immersed for 1 week in artificial seawater (Fig. 2). Although the potentials between different positions on the nodules were highly variable, mean background-corrected potentials of up to 0.24 V were found (Fig. 2), and potentials reached a maximum of 0.95 V on the surface of some nodules (Extended data Table 4). High voltages (~0.6 V) were also observed at 5ºC (pers. obs.), which indicate that high potentials can also exist under cold-water conditions. Based on these studies and measurable DOP being observed in nodule-only *ex-situ* incubations (Extended Data Fig. 4), we theorize that the DOP resulted, at least in part, from seawater electrolysis driven by electrical potentials on the surface of the nodules as well as their high Mn- and Fe-oxide and transition metal make-up that increased the electrical conductivity and reduced the voltages required for the OER. This hypothesis is additionally supported by the significant positive correlation between the total O_2 change and the average surface area of the nodules, possibly due to larger nodules having a higher abundance of anode and cathode sites. Evolution of H_2 during seawater electrolysis could also explain the high rates of chemoautotrophy observed in polymetallic nodule covered sediments in the UK1 and OMS license areas that have not been reconciled to electron donor fluxes resulting from C_{org}-remineralization[6].

Understanding the role of electrolysis in DOP and the importance of DOP in abyssal ocean ecology must be a research priorities moving forward, as well as assessing its importance in connecting polymetallic nodules and seafloor ecological processes. In the present day, DOP may help partly explain the high abundance of epifauna found living on manganese nodules in the central abyssal Pacific[23], inviting the urgent investigation of how removal of potential oxygenic substrates would affect deep-sea polymetallic nodule ecosystems. Future studies of DOP in the deep sea might also shed light on broader relationships that are known to exist between manganese-oxide deposition, biological evolution, and the oxygenation of the Earth[24,25].

References

1. Jorgensen, B.B. et al. Sediment oxygen consumption: role in the global marine carbon cycle. *Earth-Sci. Rev.* **228**, 103987 (2022).
2. Keeling, R.F. et al. Ocean deoxygenation in a warming world. *Annu. Rev. Mar. Sci.* **2**, 199–229 (2010).
3. Yamamoto, A. et al. Global deep ocean oxygenation by enhanced ventilation in the Southern Ocean under long-term global warming. *Global Biogeochem. Cycles.* **29**, 1801–1815 (2015).
4. Smith Jr, K.L. et al. Climate, carbon cycling and deep-ocean ecosystems. *Proc. Natl. Acad. Sci. USA.* **106**, 19211–19218 (2009).
5. Smith Jr. K.L. et al. Large salp bloom export from the upper ocean and benthic community response in the abyssal northeast Pacific: Day to week resolution. *Limnol. Oceanogr.* **59(3)**, 745-757 (2014).
6. Sweetman, A.K. et al. Key role of bacteria in the short-term cycling of carbon at the abyssal seafloor in a low particulate organic carbon flux region of the eastern Pacific Ocean. *Limnol. Oceanogr*. **64**, 694–713 (2019).
7. Mewes, K. et al. Diffusive transfer of oxygen from seamount basaltic crust into overlying sediments: an example from the Clarion–Clipperton Fracture Zone. *Earth Planet. Sci. Let.* **433,** 215-225 (2016).
8. Kuhn, T. et al. Widespread seawater circulation in 18–22 Ma oceanic crust: Impact on heat flow and sediment geochemistry. *Geology*, **45(9)**, 799-802 (2017).
9. Kraft, B. et al. Oxygen and nitrogen production by an ammonia-oxidizing archaeon. *Science*. **375 (6576)**, 97-100 (2022).
10. Ruff, S.E. et al. Hydrogen and dark oxygen drive microbial productivity in diverse groundwater ecosystems. *Nat. Comm.* **14(1)**, 3194 (2023).
11. Zhang, D. et al. Microbe-driven elemental cycling enables microbial adaptation to deep-sea ferromanganese nodule sediment fields. Microbiome. **11**, 160 (2023).
12. Volz, J.B. et al. Alpha radiation from polymetallic nodules and potential health risks from deep-sea mining. *Sci. Rep.* **13**, 7985 (2023).
13. D'Hondt, S. et al. Subseafloor life and its biogeochemical impacts. *Nat. comm.* **10**, 1–13 (2019).
14. Sauvage, J.F. et al. The contribution of water radiolysis to marine sedimentary life. *Nat. comm.* **12**, 1–9, (2021).
15. Hiroki, A. et al. Hydrogen peroxide production in the radiolysis of water with high radical scavenger concentrations. *J. Phys. Chem. A.* **106**, 9352–9358 (2002).
16. Ershov, B.G. & Gordeev, A.V. A model for radiolysis of water and aqueous solutions of H_2, H_2O_2 and O_2. *Radiation Phys. Chem.* **77(8)**, 928-935 (2008).

17. Ershov, B.G. Radiation-chemical decomposition of seawater: The appearance and accumulation of oxygen in the Earth's atmosphere. *Radiation Phys. Chem.* **168**, 108530 (2020).
18. Dresp, S. et al. Direct electrolytic splitting of seawater: Opportunities and Challenges. *ACS Energy Lett.* **4**, 933−942 (2019).
19. He, Y. et al. Recent progress of manganese dioxide based electrocatalysts for the oxygen evolution reaction. *Ind. Chem. Mater.* **1**, 312 (2023).
20. Kuhn, T. et al. "Composition, formation, and occurrence of polymetallic nodules" in Deep-sea mining, R. Sharma, Ed. (Springer, Cham, 2017), pp. 23-63.
21. Tian, L. Advances in manganese-based oxides for the oxygen evolution reaction. *J. Mater. Chem. A.* **8**, 14400 (2020).
22. Teng, Y. et al. Atomically thin defect-rich Fe–Mn–O hybrid nanosheets as highly efficient electrocatalysts for water oxidation. *Adv. Funct. Mater.* **28**, 1802463 (2018).
23. Vanreusel, A. et al. Threatened by mining, polymetallic nodules are required to preserve abyssal epifauna. Sci. Reports. **6**, 26808 (2016). DOI: 10.1038/srep26808.
24. Robins, L.J., et al. Manganese oxides, Earth surface oxygenation, and the rise of oxygenic photosynthesis. *Earth Sci. Rev.* **239**, 104368 (2023).
25. Chyba, C.F. & Had, K.P. Life without photosynthesis. *Science*. **292(5524)**, 2026-2027 (2001).

Acknowledgements

We would like to thank Scott Wilson, Ebbe Holsting, Frazer Mann and Lewis Carrera at Maersk Supply Service, the captain and crew of the research vessels '*Maersk Launcher*' and '*Island Pride'* for all their help preparing for the research expeditions and their excellent assistance at sea. We are grateful to Rory Davis for help with the lander deployments and Dominique Anderson, Mariana Delgado, and Dr. Marta Cecchetto for help at sea. We thank Yasheng Maierhaba, Claire Momjian and Akshata Shukla for their assistance with lab-based molecular analyses and Ralph Merrifield for his help with the electrochemistry analysis. We would like to acknowledge and give our thanks to Katie M. Allen, Dr. Michael Clarke, Antony O'Sullivan, Patrick Clarke, Dr. Leigh Marsh, and Dr. Jason Smith for helping to initiate the research, as well as the Metals Company for funding this research as part of their environmental impact assessment of the NORI-D exploration license area in the Clarion-Clipperton Zone.

Funding

The work was funded by The Metals Company Inc. through its subsidiary Nauru Ocean Resources Inc. (NORI). NORI holds exploration rights to the NORI-D contract area in the CCZ and is regulated by the International Seabed Authority and sponsored by the government of Nauru. UK Seabed Resources funded the research expedition to the UK1 and OMS license areas in 2015, and the Gordon and Betty Moore Foundation provided funding for the research cruise to APEIs 1, 4, and 7 in 2018. A.K. Sweetman acknowledges research support from the NERC SMARTEX (Seabed Mining And Resilience To Experimental impact) project (grant number NE/T003537/1) and the EC project iAtlantic (grant number 818123).

Author contributions

A.K.S., C.W., and W.B.H generated the funding. A.K.S. conceived the study and led the benthic chamber lander investigations with A.J.S. A.K.S., A.J.S., D.d J., C.A., and J.J.M. conducted the Winkler analysis and *ex-situ* core incubations. A.K.S., A.J.S., D.d J., and T.H. carried out the *in-situ* oxygen optode calibrations and analysis. M.S., P.S., and J.J.M. led the microbiology analysis, while P.S., and R.L.E. undertook the radioactivity measurements and radiolysis calculations. A.K.F., S.F., T.K., and A.K.S. did the solubility assessments and F.G. and A.K.S. undertook the electrochemistry measurements. A.K.S., J.J.M. and W.B.H. drafted the manuscript, and all authors contributed further ideas and approved the final version.

Online methods

Benthic chamber lander deployments and chamber-derived O_2 flux measurements - A benthic chamber lander was deployed in the NORI-D license area six times in May-June 2021 (5D cruise), five times in November-December 2021 (5E cruise) and five times in August-September 2022 (7A cruise) (Extended Data Fig. 1 and Table 1). The lander (KUM GmbH) comprised three independent, autonomous, square benthic chambers (484 cm^2) that were separated by approximately < 0.5 m. The lander was deployed with a USBL so accurate positioning and depth information could be gathered. After arriving at the seafloor, the lander waited for 0.07-1.34 d (due to deployment and recovery constraints) before the chambers were pushed into the sediment, creating an enclosed microcosm of the benthic ecosystem. Ten minutes into the incubation period, the enclosed chambers were injected with approximately 50 mL of one of three solutions: 1) 0.45-µm filtered, cold surface seawater containing 79.2 mg of freeze-dried *Phaeodactylum tricornutum* algae, 2) 32µM Na_2HCO_3 and 40 µM NH_4Cl dissolved in cold artificial seawater (salinity 35), and 3) 0.45-µm filtered, cold surface seawater. On some occasions, the injection mechanism failed allowing the response to control (no injection) conditions to be measured. *P. tricornutum* algae was selected

238 in the dead-algal biomass treatments because it belongs to a widely distributed diatom genus that occurs throughout the Pacific Ocean[26]. The seafloor in the study area had a temperature of 1.6ºC ± 0.006ºC (SE, n = 28) and a pH of
240 7.41 ± 0.05 (SE, n = 17). Immediately after the injection, the overlying water was mixed with a submersible stirrer at 60 rpm for one minute before the stirrer was turned off that allowed any particulate substrates to settle for one
242 hour. After one hour, the stirrer was then turned on again and the chamber waters gently stirred for the remainder of the experiments. The stirring mechanism in the benthic chambers generated a sufficiently thin diffusive boundary
244 layer (474 μm) and low static differential pressure at the sediment-water interface (0.4 Pa)[27]. Thus, there would be a low risk of creating stirrer-induced pressure effects on fluxes[27]. Moreover, intercalibration exercises have shown
246 no statistically significant difference in measured O_2 fluxes between ours and 13 other benthic chamber systems[27]. During the 5E expedition, the stirrers were programmed to continually stir the overlying water even after injection.

248 The syringe samplers removed approximately 50 mL of seawater from the water phase of each chamber at 0.1, 3, 9, 28, 38 and 47 hours into the incubation experiment. Oxygen optodes (CONTROS HydroFlash O_2 manufactured
250 by Kongsberg Maritime Contros GmbH) were mounted in the lid of each chamber and logged O_2 concentrations in the chamber every 10 seconds throughout each experiment. Two days prior to the first lander deployment of each
252 cruise, the optodes underwent a two-point, multi-temperature calibration using 0 and 100 % O_2 calibration solutions at 1.2, 7, 18 and 30 °C following the recommendations of Bittig et al. (ref. 28). On the 5D cruise, we also calibrated
254 the sensors 2 d after the last lander experiment so we could estimate optode drift, which was negligible (0.27 μmol L^{-1} d^{-1}) over the course of the 6-week cruise. The 0 % and 100 % O_2 saturation solutions were created by bubbling
256 0.45-μm filtered surface seawater in a bottle sitting in a water-chilling/ heating unit with N_2 gas (0 %) or an aquarium air bubbling unit (100 %) for 30 minutes. The O_2 concentration of the calibration solutions was confirmed in
258 triplicate by Winkler titration. After incubating seafloor sediments for 47 hours, the lander chambers were closed by a shutter door at the base of the chambers and the chambers were then pulled slowly out of the sediment, which
260 took one hour. The lander was then recalled from the seafloor by an acoustic signal approx. 10 minutes after the chambers had been retrieved from the sediment. In eight instances, the lander program did not finish, and the doors
262 did not shut preventing the sampling of sediment and determination of the volume of the water phase in the chambers (Extended date Table 2). Once the lander was back and secured on deck, the chambers were opened and the volume
264 of water above the sediment-water interface was removed via siphoning into a bucket, which was then measured using a measuring flask. The distance from the top of the sediment to the base of the chamber lid was also measured
266 in 4 places to get an accurate water depth for water volume estimates. Whenever possible, a photograph was then taken of the chamber sediment and nodules from directly above the opening of the chamber. All syringes containing
268 water samples were removed and taken to the shipboard lab for immediate processing or stored in a cold lab (4 ºC) prior to processing. The optodes were removed and their onboard data downloaded to a computer that was backed
270 up to two hard drives. Finally, the nodules were removed from the chambers, and washed of attached organic debris with cold (4ºC), 0.45-μm filtered surface seawater and placed in sterile Whirlpak® bags to be weighed in the
272 laboratory later. Polymetallic nodule abundance in the chambers was 55 ± 4 m^{-2}.

Unfiltered syringe sample seawater was carefully transferred from each 50 mL syringe to a 12 mL exetainer via a
274 10 cm tube attached to the syringe nozzle, ensuring no air bubbles were introduced. The water was then immediately fixed with 150 μl of 3M $MnCl_2$•$4H_2O$ and 150 μl of 8M NaOH + 4M NaI solution. The sample was then mixed
276 thoroughly using a glass bead placed in the exetainer, and then placed in the dark in a 4 ºC refrigerator for 30 - 45 minutes to allow the precipitate to settle. Once the precipitate had sedimented, the exetainers were shaken again and
278 left for two-three hours before Winkler titrations were performed. All titrations were completed within 12 hours after sampling to determine dissolved O_2 concentrations. Each Winkler sample (approx. 5 mL) was titrated twice,
280 and duplicate measurements showed minor differences in O_2 concentration (5D cruise error: 3.5 ± 0.3 μmol l^{-1}, n = 71; 5E cruise error: 1.3 ± 0.2 μmol l^{-1}, n = 69; 7A cruise error: 2.8 ± 0.4 μmol l^{-1}, n = 84). All syringe samples were
282 fixed for Winkler analysis within 30 - 45 minutes of the lander arriving at the surface, and the order that the syringe samples were sampled was randomized to counter the potential effects of delayed analysis. Winkler O_2
284 concentration data was averaged for each syringe sample. The O_2 concentrations estimated by Winkler analysis were 22 ± 1 % (n = 42, SE, 5D cruise), 8 ± 4 % (n = 39, SE, 5E cruise), and 24 ± 2 % (n = 40, SE, 7A cruise) lower
286 than the concentrations measured by the optodes at the same time point in the same incubations. This difference is most easily explained by the efficient out-gassing of supersaturated O_2 caused by depressurization and warming of
288 the externally mounted syringes (whose samples were used for Winkler analyses) during the lander recovery to the surface.
290
Back on shore, the correct O_2 concentration values were calculated following Bittig et al. (ref. 28) from the optode,
292 calibration and *in-situ* pressure data that was derived from the USBL seafloor depth. Timestamps in the optode data were compared to the lander computer program times so the optode readings could be aligned to the schedule
294 of the chamber experiment. The total change in O_2 concentration in each chamber was then calculated from the

volume of the water phase above the sediment, and the difference in O_2 concentration from when the chambers started to seal off the sediment to the point when the maximum O_2 concentration was reached.

Benthic O_2 microprofiling – Benthic O_2 microprofiles were made during lander deployments AKS313, AKS316, AKS318, and AKS321 during the 5E cruise using a UNISENSE deep-sea microprofiling unit mounted < 0.5 m from the benthic chambers. The microprofiles were made using 20 cm O_2 microsensors that penetrated the sediment in 0.05 mm steps. The microsensors were calibrated < two hours before the lander deployments at *in-situ* temperature (1.6ºC) at 0 % and 100 % O_2 saturation (see above). The micro-profiling unit was programmed to start profiling the sediment approximately nine hours after the lander reached the seafloor to reduce any disturbance (e.g., sediment resuspension and deposition) artefacts in the measurements. At each sampling depth, the microsensor stopped for five seconds before each measurement was made. The sensor then recorded five individual O_2 concentration measurements. The average of these five measurements was taken for each depth point. The sediment surface was determined manually based on the turning point in the slope of O_2 concentration with depth where O_2 started to become depleted.

Benthic chamber sediment sampling for microbiology during the 5D expedition - After the syringes for Winkler samples had been removed from the chambers, sediment samples for microbiology analysis were collected from the chambers with a pre-sterilized spatula. Approximately 50 g from each of the 0 - 2 cm and 2 - 5 cm horizons were placed in separate sterile Whirlpak bags and then transferred to a -80 ºC freezer. Samples were then shipped on dry ice to Laragen, Inc. (Culver City, CA), where DNA was extracted using a proprietary in-house method. The V4 region of 16S rRNA genes were amplified using the Earth Microbiome Project protocol[29] with the 515F (5′-GTGYCAGCMGCCGCGGTAA[30]) and 806R (5'-GGACTACNVGGGTWTCTAAT[31]) primers. After amplification, 100 ng of PCR product was purified, quantified, and sequenced using a PE150 kit on a MiSeq sequencer. Sediment samples were only collected during the 5D field expedition.

Microbiome data processing - Raw fastq files were processed using a custom pipeline (https://github.com/Boston-University-Microbiome-Initiative/BU16s) built with QIIME 2020.2 (https://www.nature.com/articles/s41587-019-0209-9). Adapter sequences (forward: GTGYCAGCMGCCGCGGTAA, reverse: GGACTACNVGGGTWTCTAAT) were removed using cutadapt (times 2, math-read-wildcards True, match-adapter-wildcard True, minimum-length 50) (doi:10.14806/ej.17.1.200), read truncation positions were determined by mineer (see more below), amplicon sequence variants (ASVs) were generated using dada2 (trunc-len-r[30]) (doi:10.1038/nmeth.3869), and ASVs were clustered to 99% identity with the SILVA 132 database (https://academic.oup.com/nar/article/42/D1/D643/1061236) using the vsearch cluster-features-closed-reference (doi:10.7717/peerj.2584).

Sequence truncation - Due to drops in sequencing quality, all reverse reads were truncated by 49 bases (from a length of 301 to 252). This truncation length was determined by minEER (minimization of expected error rate) with minimum allowed length (MAL) = 100, maximum allowed expected error rate (MAE) = 0.01, and number of sampled reads (NREADS) = 5000. minEER is a novel algorithm that optimally truncates quality-annotated sequencing reads by maximizing sequence length for a given mean PHRED quality score (or expected error rate). minEER is intended to be a quantitative alternative to current sequence truncation techniques, which rely on qualitative assessments of sequence quality profiles. For a given sequencing read, the minEER algorithm first calculates the expected error rate of all sub-sequences of length greater than or equal to the MAL. Next, sub-sequences are filtered to those with expected error rates less than or equal to the MAE. Finally, the algorithm reports the longest of the sub-sequences. When a set of sequences from a single study is passed to the minEER program, NREADS sequences are sub-sampled and the median starting and ending truncation position for each sub-sampled read are used to truncate all remaining sequences. The code for installing and using minEER can be found at: https://github.com/michaelsilverstein/mineer.

Microbiome analysis – Family- and genus-level abundance was computed by summing the relative abundance of all ASVs with the same Family/ Genus classification within each sample. Spearman correlations were then computed between Family-/ Genus-level abundance and observed optode-derived total O_2 changes. Sequences have been archived at NCBI GenBank under the Bioproject ID ****.

Polymetallic nodule surface area measurements – Photographs of the surface sediment and nodules in the chambers were imported into Image J®. In a limited number of cases, the photographs could not be used because water was still present in the chamber or the camera lens fogged up due to the warm humid air on deck, which impaired the view of the nodules. After importing each image, the pixel to centimetre scale was set using the width of the chamber (22 cm) and 'Set Scale' function in Image J. The outline of each nodule in each chamber photograph was then

traced and the surface area of the nodule automatically calculated in Image J (assuming each surface nodule was flat in shape) and logged as an Image J file before being exported and saved as an Excel file.

Radiolysis O_2 production estimates - To estimate the potential radiolytic O_2 production, contributions from nodules, sediment, and seawater were considered. For seawater, published concentrations of ^{238}U, ^{235}U, ^{232}Th, ^{40}K (refs 32-36) were used (Extended Data Table 5). For nodules, ^{238}U, ^{235}U, and ^{232}Th isotopes of three nodules from chamber experiments from the 5D cruise were measured by MC-ICP-MS using previously described methods[37-39] and averaged; ^{40}K values were derived from the literature[20]. Nodule and seawater contributions were calculated using a kinetic model developed by ref. 17 that incorporates 32 reactions (Eq. 1, [ref. 16]). The nodule boundary layer was assumed to be fully integrated with the seawater, surpassing the respective ~ 23 to ~ 452 μm stopping power distance of Alpha and Beta particles used to model geologic materials[41]. Sediment radiolytic O_2 was calculated as half of the previously quantified H_2 production rates in equatorial Pacific subsurface sediment[42], given the stoichiometry of water's radiolytic decomposition (an equivalency that likely offers an over-estimate of derived O_2). Contributions from these three components (nodules, sediment, and seawater) were scaled by the benthic chamber's size and contents to produce an estimate of 0.18 μmol L^{-1} of O_2 generated over 48 hr according to the following expression.

$$[O_2]_t = [Q_{iz} \cdot E_a \cdot G(O_2) \cdot M_{O2} \cdot A_{iz}^{-1} \cdot 10^{-2}] \times (1 - e^{-\lambda t})$$

Here, $[O_2]_t$ is the mass (kg) of O_2 produced over a given time t (yr), Q_{iz} is the mass (g) of the isotope, E_a is the average energy (eV) released from the decay of one atom; $G(O_2)$ is the radiation chemical yield of molecules per 100 eV of the radiation energy; M_{O2} is the O_2 molecular mass (g), A_{iz} is the isotope atomic mass (g), and λ is the isotope-specific decay constant (yr^{-1}). The overall $[O_2]_t$ value summed the contributions from ^{238}U, ^{235}U, ^{232}Th, and ^{40}K across water, nodule, and sediment sources.

Electrochemistry measurements – Voltage potentials were measured at 165 locations on 12 nodules collected by coring in the UK1 and NORI-D license areas, and the BGR license area situated to the north of NORI-D. Potentials were measured on a Keithley DMM6500 digital multi-meter and logged directly to a computer. Prior to the potentials being measured, nodules were immersed for seven days in Instant Ocean artificial seawater (salinity 35). To measure the potentials, the electrodes (platinum wire, 99.9% purity) were first washed in perchloric acid, rinsed in Milli Q water, and then dried before being attached to alligator clamps attached to the multi-meter. The platinum wires were first immersed in Instant Ocean artificial seawater in a glass petri dish to measure background voltages (0.003 ± 0.001 V, SE, n = 17) until stable. Once stable, a nodule was immersed in the petri dish and the platinum probes placed at different locations on the nodule and the voltages recorded for 1-2 mins. This procedure was repeated up to 20 times in different regions of the nodules depending on their size. Measurements were undertaken on 12 nodules at 21ºC (n = 147) and a single control rock composed of metamorphosed carbonate (n = 10). To assess the effect of temperature on the voltage potentials, two nodules from UK1 were retested after being cooled to 5ºC (n = 18) by placing them in Instant Ocean water in a refrigerator overnight. Voltage potentials (n = 20) between two nodules were also measured using four nodules collected from UK1. Voltages of the nodules made during each measurement were averaged and corrected for the background voltages measured with only Instant Ocean seawater.

Geochemistry modelling – The chemical stability and solubility of manganese (IV) oxide (birnessite) to dissolved Mn^{2+} as a function of pH and O_2 activity was modelled using the Geochemist Workbench Professional (Vers. 12) software, with the in-build and internally consistent THERMO database. The conditions used for generating the phase diagram (Extended data Fig. 5) represent bottom seawater as measured in the eastern CCZ with a temperature of 1.6ºC and chlorine and manganese concentrations of 0.55M Cl and 2^{e-10}M Mn, respectively.

Ex-situ core incubations – Opportunistic replicated *ex-situ* experiments were undertaken during the 5D cruise using sediment cores retrieved by a multi-corer (MUC) from the PRZ area in NORI-D (Extended data Fig. 1). Immediately after the MUC arrived back at the surface, a bung was placed at the bottom of the cores and then they were transferred to a cold lab held at *in-situ* temperature. The cores were then exposed to the following 5 treatments (administered using a 60-mL syringe) which included 1) Na_2HCO_3 (0.3 μM final conc. n = 3), (2) NH_4Cl (10 μM final conc. n = 3) and (3) NH_4Cl (50 μM final conc. n = 3), (4) 0.3 μM Na_2HCO_3 + 10 μM NH_4Cl (final conc. n = 3) and 5) $HgCl_2$ (1.1 μM final conc. n = 3). No-injection controls (n = 3) were also performed as well as two separate core experiments in which four nodules were incubated for 48 hours by themselves with no additions. After addition, the water phase of each core was stirred, and a 50-mL sample of top water was carefully taken by syringe for Winkler analysis (as above). Due to the low permeability of the sediment, it is unlikely that much of the subsurface volume in the sediment incubations was exposed to the added nutrients / chemicals. Stoppers were then placed on the top of the cores, ensuring no air bubbles were present. The stoppers were secured tightly with

electrical tape, and the cores fully submerged in a large bucket containing 0.45-µm filtered, cold surface seawater (salinity 35). The bucket was covered with 5 black plastic bags and secured in the cold room with the lights turned off. After 48 hours, the cores were removed from the bucket, the tape was removed from the stoppers, and the cores were inspected for the presence of air bubbles. Only one core, a $HgCl_2$ treatment, had an air bubble beneath the bung. This core was rejected from further analysis, leaving $n = 2$ for this treatment. The other cores were then re-sampled for dissolved O_2 by removing the top stopper, quickly mixing the water phase, and then taking another sample for Winkler analysis, which was analysed as before. Core-specific water volume measurements were used together with the change in O_2 concentration to calculate the total O_2 change per core.

To determine if our *ex-situ* DOP detection was affected by the diffusion of O_2 from the atmosphere into the core tube, two controls were performed: a shipboard test with an O_2 microprofiler, and a lab-based test using the Winkler method. Shipboard, a clean core tube was filled with Milli-Q water and sparged with N_2 for 10 minutes prior to beginning the test. A Metrohm 8663 Multimeter was inserted through a predrilled hole in the rubber stopper, allowing for O_2 concentration to be recorded every 5 seconds. An increase from 39 to 69 µmol L^{-1} was observed over ~ 5 hr, corresponding to a rate of 0.14 mmol m^{-2} d^{-1} or 4 % of the 3.5 mmol L^{-1} d^{-1} mean DOP measured in the *ex-situ* experiments. Because of the hole in the stopper and the hypoxic nature of the experiment, this shipboard control represents a conservative view of the influence of O_2 diffusion into the incubation tubes (e.g., there are compelling reasons to believe it produced an over-estimate).

Back in the home laboratory, three of the original core tubes were filled with 4°C, 0.2 µm-filtered artificial seawater (salinity 35) and sparged with N_2 for eight minutes through a filtered pipette tip to achieve an initial dissolved O_2 concentration of ~100 µmol L-1 (e.g., the approximate starting O_2 concentrations for the shipboard experiments). The tubes were sealed with rubber stoppers and electrical tape, being careful to avoid bubble formation. They were then submerged in a 32-gallon plastic garbage can of unfiltered seawater (O_2 concentration: 228.12 µmol L^{-1}) in a dark cold room (8 °C) for 48 hours. After the incubation, the tubes were quickly unsealed and analysed one at a time to prevent additional O_2 dissolution from the air. A 50-mL sterile syringe was used to slowly collect 10-mL of seawater from the centre of the core tube, being sure to avoid bubble entrainment in the syringe. The sample was carefully expelled into a 10-mL reaction vial and fixed using the adjusted values for a 10-mL sample according to a volume-scaled Winkler Titration protocol[43] and the reagents from the LaMotte Dissolved Oxygen Test Kit. The fixation of each collected sample was done in less than two minutes in a fume hood. Dissolved O_2 increased by 0.11 mmol m^{-2} d^{-1} during the 48 hr, which corresponds to between 3.2 % of the mean DOP rate observed in the *ex-situ* experiments (3.5 mmol L^{-1} d^{-1}). Both of our control experiments thereby provide high confidence that the diffusion of external O_2 into the core tubes does not account for the observations of O_2 production in the *ex-situ* core incubations that were conducted during the 5D cruise.

Calculations to quantify d*iffusion of O_2 from the polyoxymethylene chambers and lids* – Oxygen diffusion from the polyoxymethylene plastic chambers was estimated from Stephens[44] who calculated that 20.66 µmol L^{-1} of O_2 could diffuse out of 428 cm^2 of polyoxymethylene plastic when immersed for 48 hours in hypoxic water (O_2 diffusion rate: 0.02 µmol O_2 cm^{-2} d^{-1}). To determine the total area of plastic that would be available for diffusion (869 – 1584cm^2), we added the surface area of the lid to the surface area of the 4 walls that would be exposed at the seafloor (based on the depth of the water phase – see above). The minimum and maximum areas available for diffusion were multiplied by 0.02 µmol O_2 cm^{-2} d^{-1} to estimate that 41.9 – 76.5 µmol O_2 L^{-1} would diffuse out of the polyoxymethylene chamber walls and lid in 48 hours under hypoxic conditions. As the water enclosed by the chambers was always well oxygenated (Fig. 1), O_2 diffusion from the plastic would be less than under hypoxic conditions. Thus, we are highly confident that O_2 leakage from the plastic chambers could not replicate the high O_2 concentration seen in some of our experiments (Fig. 1).

In-situ benthic chamber incubations in APEIs 1, 4, and 7 and the OMS and UK1 license areas - During a cruise to the Ocean Minerals of Singapore (OMS) and UK1 license areas in February/ March 2015 on the RV "*Thomas G. Thompson*", and the western CCZ on the RV "*Kilo Moana*" in June 2018, 36-hr in-situ benthic chamber incubations were carried out at the abyssal seafloor (Extended data Fig. 1) and collected optode data in an identical way to the NORI-D incubations. The O_2 concentrations recorded by the optodes in the 2015 and 2018 experiments were derived from factory calibrations undertaken 4-6 months prior to the expeditions as *in-situ* temperature could not be replicated onboard during the optode calibration process. As such, the profiles shown in Extended data Fig. 3 only show the relative change in O_2 concentration in the chambers over time.

Online methods references

26. De Martino, A. et al. Genetic and phenotypic characterization of *Phaeodactylum tricornutum* (Bacillariophyceae) accessions. *J. Phycol.* **43**, 992–1009 (2007).

27. Tengberg, A. et al. Intercalibration of benthic flux chambers II. Hydrodynamic characterization and flux comparisons of 14 different designs. Mar. Chem. **94**, 147-173 (2005).
28. Bittig, H.C. et al. Oxygen optode sensors: principle, characterization, calibration, and application in the ocean. *Front. Mar. Sci.* **4**, 429 (2018).
29. Caporaso J.G. et al. Earth microbiome project: EMP 16S Illumina amplicon protocol. (2018).
30. Parada, A.E. et al. Every base matters. assessing small subunit rRNA primers for marine microbiomes with mock communities, time series and global field samples. *Environ. Microbiol.* **18(5)**,1403-1414 (2016).
31. Apprill, A. et al. Minor revision to V4 region SSU rRNA 806R gene primer greatly increases detection of SAR11 bacterioplankton. *Aquatic Microbial Ecol.* **75(2)**, 129-137 (2015).
32. Choppin, G. et al. Eds. Radiochemistry and nuclear chemistry. (Elzevier, 2002), 709pp.
33. Katz, J.J. et al. Eds. The chemistry of the actinide elements. 2nd Edition (Springer, 1986). 912pp.
34. Lide, D.R. Ed. CRC handbook of chemistry and physics (Vol. 85). (CRC press, 2004), 2712pp.
35. Nier, A.O. A redetermination of the relative abundances of the isotopes of carbon, nitrogen, oxygen, argon, and potassium. *Physical Rev.* **77(6)**, 789 (1950).
36. Stumm, W and Morgan, J.J. Aquatic Chemistry: An introduction emphasizing chemical equilibria in natural waters. 2nd Edition (John Wiley & Sons Ltd., New York. 1981), 780pp.
37. Cheng H. et al. Improvements in ^{230}Th dating, 230Th and 234U half-life values, and U–Th isotopic measurements by multi-collector inductively coupled plasma mass spectrometry. *Earth Planet. Sci. Let.* **371**, 82-91 (2013).
38. Edwards, R.L. et al. ^{238}U, ^{234}U, ^{230}Th, ^{232}Th systematics and the precise measurement of time over the past 500,000 years. *Earth Planetary Sci. Let*. **81 (2-3)**,175-192 (1987).
39. Shen C.C. et al. Uranium and thorium isotopic and concentration measurements by magnetic sector inductively coupled plasma mass spectrometry. *Chem. Geol.* **185 (3-4)**, 165-178 (2002).
40. Kuhn, T. et al. "Composition, formation, and occurrence of polymetallic nodules" in Deep-sea mining, R. Sharma, Ed. (Springer, Cham, 2017), pp. 23-63.
41. DeWitt, J. et al. The effect of grain size on porewater radiolysis. Earth. Space. Sci. **9(6)**, e2021EA002024 (2021).
42. Blair, C.C. et al. Radiolytic hydrogen and microbial respiration in subsurface sediments. *Astrobiol.* **7(6)**, 951-970 (2007).
43. Shriwastav, A. et al. A modified Winkler's method for determination of dissolved oxygen concentration in water: Dependence of method accuracy on sample volume. *Measurement.* **106**, 190–195 (2017).
44. Stevens, E.D. Use of plastic materials in oxygen-measuring systems. *J. Appl. Physiol.* **72**, 801–804 (1992).

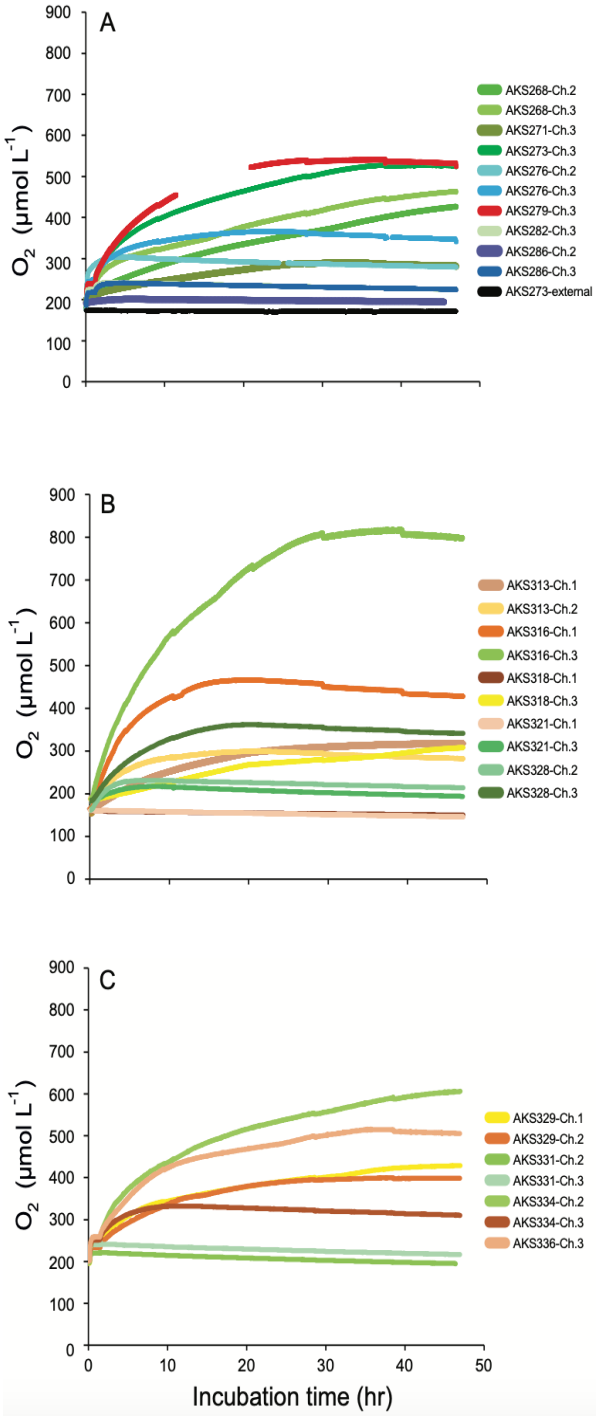

Figure 1. Oxygen concentrations (µmol L^{-1}) measured by calibrated O_2 optodes through time (hr) in the different benthic chamber incubations during the *in-situ* benthic chamber lander deployments made during the 5D (A), 5E (B) and 7A (C) cruises to the NORI-D license area (Extended data Figure 1). Nodules were present in all incubation experiments. The green hue, blue hue, and red lines in the 5D figure (A) denote dead-algal biomass, DIC + NH_4^+, and filtered seawater treatments, respectively. The gap in the optode data in AKS279-Ch.3 was caused by the optode periodically not logging data. The black line indicates ambient O_2 concentration measured on the outside of the benthic chambers during AKS273 on the 5D cruise. The green and yellow hue lines in the 5E (B) and 7A (C) figures denote the dead-algal biomass and control (no injection) treatments, respectively. The minor drops seen in some of the O_2 concentration profiles at 28, 38 and 47 hr are caused by the dilution of the chamber water with 50-mL of seawater that was entrained from the outside into the chamber through a 1.5m (0.25cm dia.) open tube when the syringe sampler collected seawater samples from within the chamber. The constant O_2 concentration measured during the first 2 hr of the 5D and 7A experiments was due to the stirrers being turned off for 1 hr to allow the

substrates (e.g., dead-algal biomass) to sink to the sediment surface. Stirrers were turned on during the 5E expedition from the moment the lander was deployed until the lander returned and power to the stirrers was disconnected.

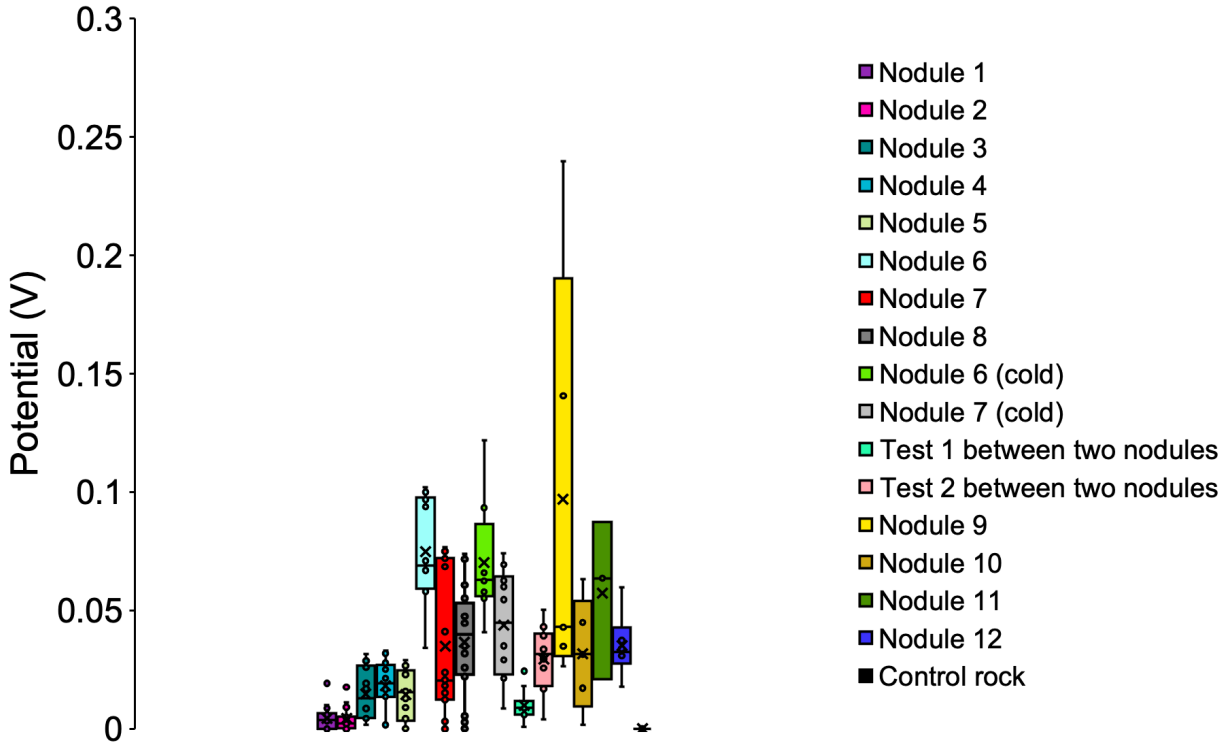

Figure 2. Box-whisker plots of background-corrected voltage potentials (V) for nodules collected from the NORI-D (1-5), UK1 (6-8), and the BGR (9-12) license areas. Potentials were measured at 21ºC (nodules 1 – 12) and 5ºC (nodules 6 and 7 cold), as well as between two different UK1 nodules (Tests 1 and 2), and across the surface of a metamorphosed carbonate rock (control). Means are designated by the 'x' symbol.

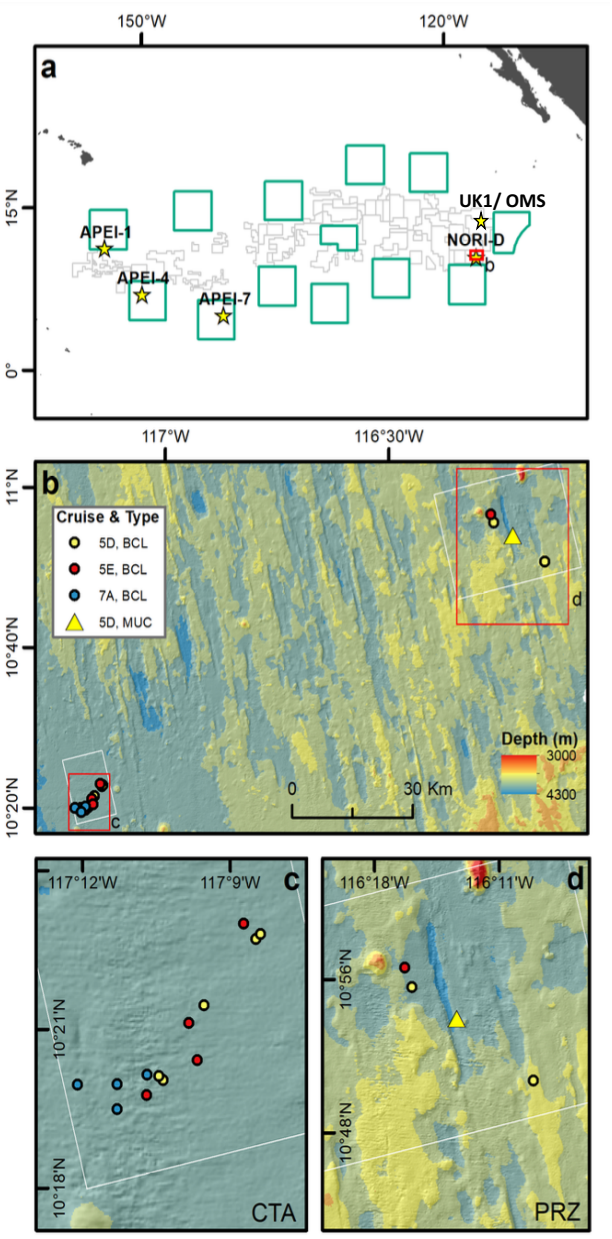

Extended date Figure 1. Benthic chamber lander (BCL) locations in APEIs 1, 4, and 7, UK1 and OMS and NORI-D (stars) and both areas (Collector Test Area or CTA and Preservation Reference Zone or PRZ) of NORI-D in the central abyssal Pacific. The deployment location for the multi-corer (MUC) that sampled sediments for the *ex-situ* experiments conducted during the 5D cruise is also shown.

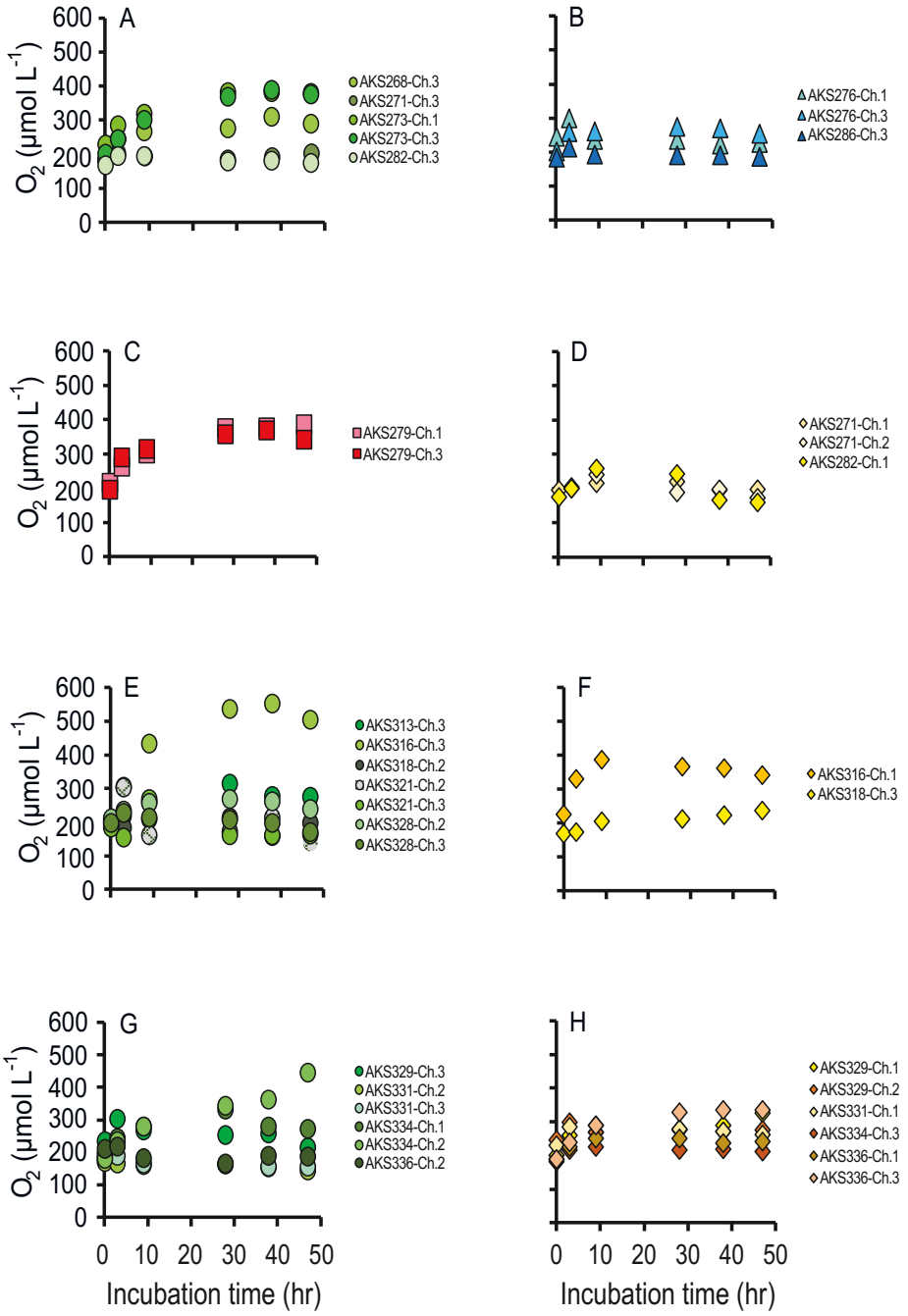

Extended data Figure 2. Mean O_2 concentration (µmol L^{-1}) measured by micro-Winkler analysis conducted on water samples that were collected periodically from the chambers through time (hr) under different treatments. The treatments were dead-algal biomass during expeditions 5D (A), 5E (E), and 7A (G), DIC + NH_4^+ during expedition 5D (B), 0.45-µm filtered seawater during expedition 5D (C), and control (no injection) during expeditions 5D (D), 5E (F), and 7A (H). Each datapoint is the mean of two Winkler measurements.

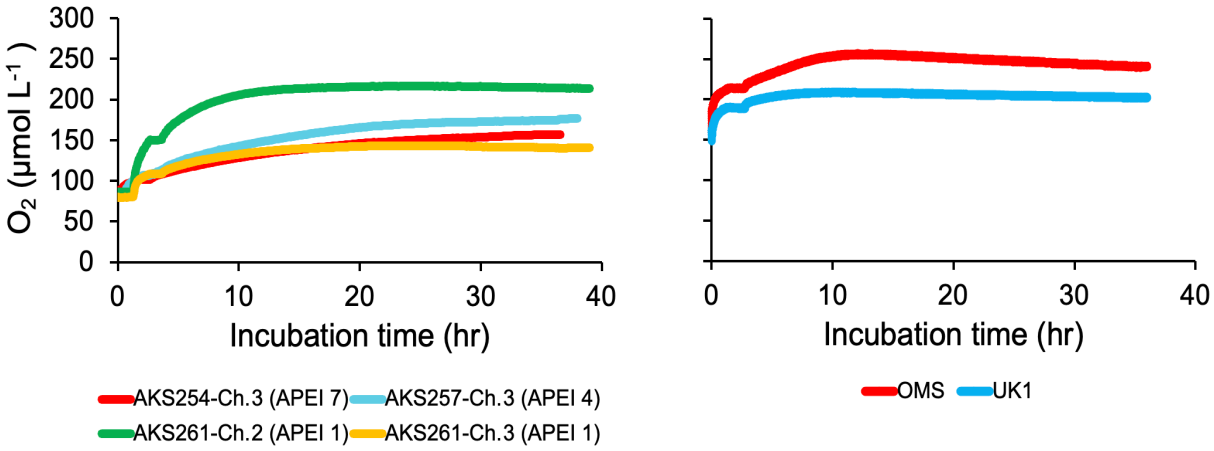

Extended data Figure 3. Oxygen optode readings through time (hours) from 36-hour abyssal (4037-5216m) *in-situ* benthic chamber lander experiments conducted in the UK1 and OMS licence areas in 2015 and APEIs 1, 4, and 7 in the western CCZ in June 2018. The optode readings were derived from the factory calibration procedure, so only relative changes in O_2 concentrations can be interpreted.

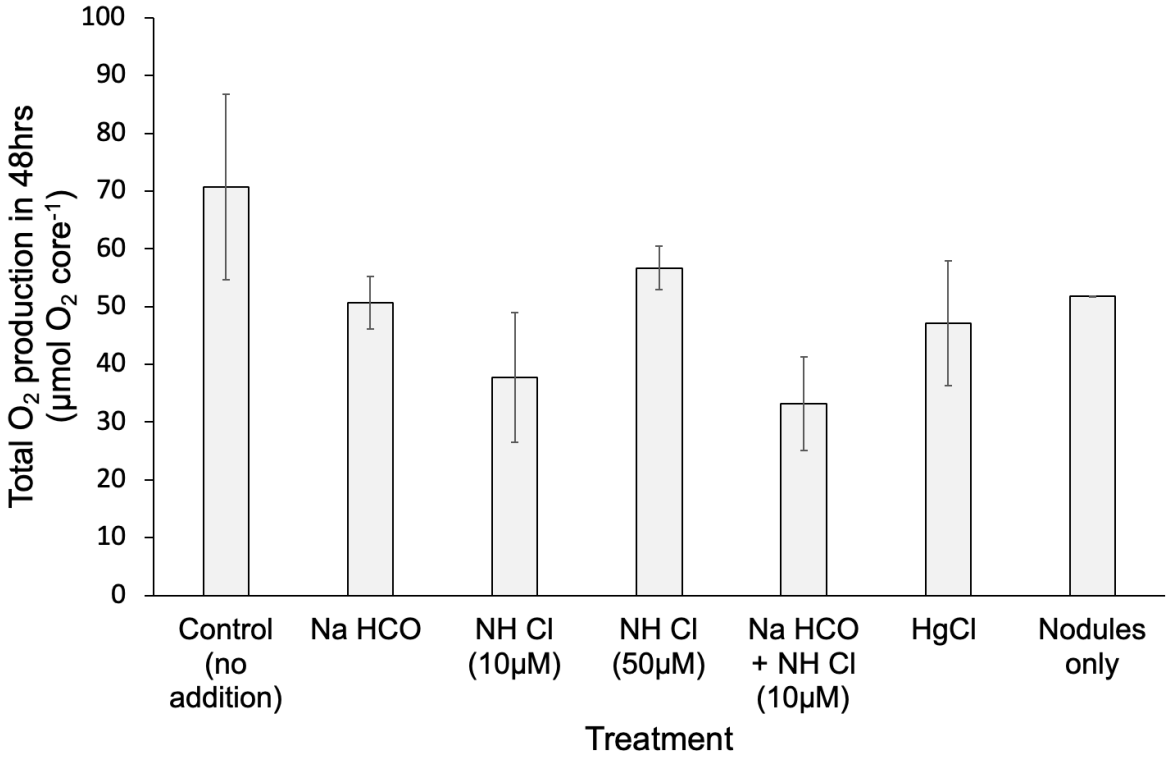

Extended data Figure 4. Mean total O_2 production (µmol O_2 core^{-1}) measured on sediment cores exposed to a variety of treatments during 48-hour *ex-situ* incubations that were carried out on the ship at *in-situ* temperature and in the dark during the 5D cruise. Oxygen production was determined from the difference in O_2 concentration of the water phase overlying the sediment between t = 0 hours and 48 hours and accounting for the core volume. Error bars refer to 1 SE (n = 3), except for the mercury chloride and nodule only treatments that shows the range around the mean (n = 2). For the nodule only treatment, the range is 0.003µmol O_2 core^{-1}.

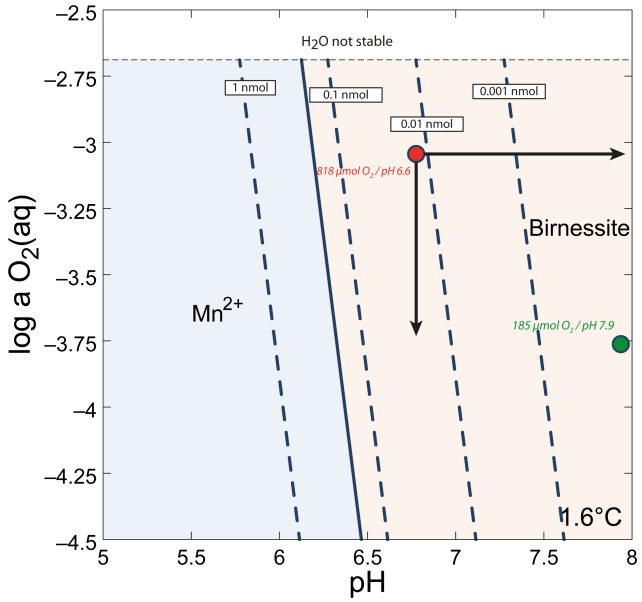

Extended data Figure 5. The phase stability and solubility of birnessite (manganese [IV] oxide) in seawater as a function of O_2 activity and pH at a temperature of 1.6° C, 0.55M Cl, and $2e^{-10}$M Mn. The bold black line illustrates the phase boundary between birnessite and dissolved Mn^{2+}; the dashed lines the solubility of birnessite into seawater. The green point indicates the predominant manganese form that would be experienced at the highest pH that was measured in MUC cores, and the lowest O_2 condition (average bottom seawater); the red point indicates the predominant manganese form at the lowest pH (measured in MUC cores) and highest O_2 concentration measured in the *in-situ* benthic chamber experiments at NORI-D with the arrows showing their range. Under the latter conditions, a vanishing small amount of birnessite would dissolve into seawater to form Mn^{2+}.

Extended data table 1. *In-situ* benthic chamber lander deployment locations and depths from the 3 cruises to the NORI-D license area. Deployment areas are shown in Extended data Fig. 1 and are defined as the Collector Test Area (CTA) and Preservation Reference Zone (PRZ).

Cruise	Date	Lander deployment	Area	Station	Depth (m)
5D	May-June 2021	AKS268	CTA	STM-001	4285
5D	May-June 2021	AKS271	CTA	STM-001	4284
5D	May-June 2021	AKS273	CTA	STM-014	4306
5D	May-June 2021	AKS276	CTA	STM-014	4306
5D	May-June 2021	AKS279	CTA	STM-007	4280
5D	May-June 2021	AKS282	PRZ	SPR-033	4245
5D	May-June 2021	AKS286	PRZ	SPR-041	4127
5E	November-December 2021	AKS313	CTA	STM-014	4304
5E	November-December 2021	AKS316	CTA	STM-001	4285
5E	November-December 2021	AKS318	CTA	STM-007	4277
5E	November-December 2021	AKS321	CTA	STM-001	4285
5E	November-December 2021	AKS328	PRZ	SPR-033	4243
7A	August-September 2022	AKS329	CTA	TF-021	4289
7A	August-September 2022	AKS331	CTA	STM-001	4286
7A	August-September 2022	AKS334	CTA	TF-028	4278
7A	August-September 2022	AKS336	CTA	TF-021	4271

Extended data Table 2. Total oxygen change measured by O_2 optodes during the *in-situ* benthic chamber lander experiments at NORI-D. Stars (*) denote the incubations where the optodes did not start to log O_2 concentrations immediately or stopped logging before 47 hr meaning the total O_2 change could not be determined (designated by a dash [-]). The total O_2 change could also not be determined in a sub-set of experiments (designated by a dash [-]) because the chambers failed to seal sediments at the end of the experiment, which meant that the volume of water in the chamber could not be determined (designated NA) once the lander arrived back on deck. The determination of net production/ respiration dominated experiments was based on the O_2 optode profiles seen in Fig. 1.

Lander deployment	Chamber	Optode sensor	Treatment	Volume of water phase (L)	Start-End time (hr) optodes logged O_2 data	Total O_2 production in 48hrs (μmol O_2)	Weight (g) of nodules (sediment horizon)	Net production/ respiration dominated
AKS268	2	B	Dead-algal biomass	NA	0 - 47	-	-	Production
AKS268	3	A	Dead-algal biomass	3.812	0 - 47	1008	782 (0-5cm)	Production
AKS271	3	A	Dead-algal biomass	NA	0 - 47	-	-	Production
AKS273	3	A	Dead-algal biomass	4.598	0 - 47	1545	653 (0-5cm)	Production
AKS276	2	B	DIC+NH_4^+	NA	0 - 47	-	-	Production
AKS276	3	A	DIC+NH_4^+	3.933	0 - 47	671	390 (0-5cm)	Production
AKS279	3	A	Filtered seawater	4.659	0 - 47	1639	410(0-5cm)	Production
AKS282	3	A	Dead-algal biomass	4.598	0 - 47	6.050	-	Production
AKS286	2	B	DIC+NH_4^+	NA	0 - 45.48	-	-	Production
AKS286	3	A	DIC+NH_4^+	6.050	0 - 47	329	466(0-5cm)	Production
AKS313	1	B	Control (no injection)	NA	0 - 47	-	-	Production
AKS313	2	A	Control (no injection)	NA	0 - 47	-	-	Production
AKS316	1	B	Control (no injection)	2.118	0 - 47	639	512 (0-2cm)	Production
AKS316	3	A	Dead-algal biomass	2.420	0 - 47	1526	662 (0-2cm)	Production
AKS318	1	B	Control (no injection)	NA	0 - 47	-	-	Respiration
AKS318*	3	A	Control (no injection)	2.783	0.23 – 47	-	596 (0-2cm)	Production
AKS321	1	B	Control (no injection)	NA	0 - 47	-	-	Respiration
AKS321*	3	A	Dead-algal biomass	2.783	1.33 – 47	-	863 (0-5cm)	Production
AKS328	2	B	Dead-algal biomass	3.691	0 - 47	257	630 (0-5cm)	Production
AKS328	3	A	Dead-algal biomass	3.812	0 - 47	683	556 (0-5cm)	Production
AKS329	1	A	Control (no injection)	3.872	0 – 47	904	755 (0-5cm)	Production
AKS329	2	B	Control (no injection)	3.872	0 – 47	774	704 (0-5cm)	Production
AKS331*	2	A	Dead-algal biomass	2.723	0.06 – 46.45	-	704 (0-5cm)	Production

AKS331*	3	B	Dead-algal biomass	3.207	0.07 – 47	-	608 (0-5cm)	Production
AKS334	2	A	Dead-algal biomass	4.175	0 – 47	1710	667 (0-5cm)	Production
AKS334	3	B	Control (no injection)	5.143	0 – 47	652	621 (0-5cm)	Production
AKS336	3	B	Control (no injection)	4.477	0 – 47	1408	622 (0-5cm)	Production
Mean change ± SE						933 ± 132		

Extended data table 3. Theoretical diffusion times (seconds) for thin versus thick-walled bubbles at the seafloor. The theoretical time for O_2 to diffuse from a trapped air bubble at the seafloor was estimated by calculating the size of air bubble that would be required at the surface to produce the O_2 increase seen in each chamber. This was estimated from the difference between the max O_2 concentration value recorded by the optode and the initial O_2 optode reading in the chamber, the volume (L) of the water phase in the chamber and assuming air was comprised of 21% O_2. The size of the bubble at the seafloor was then computed using Boyle's law and the *in-situ* pressure calculated from the USBL depth. The O_2 concentration gradient (dC) between the bubble and the water phase of the chamber was determined from the concentration of O_2 in the theoretical bubble and the initial concentration of O_2 in the chamber. The diffusion distance (dZ) was set at 10 and 10,000 nm to calculate the diffusion times across a thick versus thin-walled bubble. The diffusion coefficient for O_2 (1.064×10^{-5} cm^{-2} s^{-1}) was calculated from the O_2 diffusion coefficient based on an *in-situ* salinity of 35 and temperature of 1.6ºC. Fick's first law of diffusion was then used to calculate the diffusion time based on the diffusion coefficient, dZ and dC.

Incubation	Time (sec) required for diffusion assuming a thick-walled (10000 nm) bubble	Time (sec) required for diffusion assuming a thin-walled (10 nm) bubble
AKS268-Ch3	1.226	0.012
AKS273-Ch3	1.411	0.014
AKS276-Ch3	1.068	0.011
AKS279-Ch3	1.442	0.014
AKS282-Ch3	0.768	0.008
AKS286-Ch3	0.854	0.009
AKS316-Ch1	1.053	0.011
AKS316-Ch3	1.407	0.014
AKS328-Ch2	0.780	0.008
AKS328-Ch3	1.080	0.011
AKS329-Ch1	1.182	0.012
AKS329-Ch2	1.122	0.011
AKS334-Ch2	1.463	0.015
AKS334-Ch3	1.061	0.011
AKS336-Ch3	1.372	0.014
Mean ± SE	1.153 ± 0.061	0.012 ± 0.001

Extended data Table 4. Minimum and maximum voltage potentials (mV) measured on the surface of the polymetallic nodules at 21ºC (nodules 1 – 12) and 5ºC (nodules 6 and 7 cold), and control rock. The voltages have not been corrected for the background voltages measured using only instant water.

Miniumum voltage (mV)	Nodule 1	Nodule 2	Nodule 3	Nodule 4	Nodule 5	Nodule 6	Nodule 6 (cold)	Nodule 7	Nodule 7 (cold)	Nodule 8	Nodule 9	Nodule 10	Nodule 11	Nodule 12	Control
Record 1	0.00	0.00	0.00	0.00	0.01	0.00	58.55	77.83	0.00	0.01	0.00	0.00	78.81	0.00	0.01
Record 2	8.97	18.45	15.48	3.03	0.00	97.30	40.90	79.56	21.65	25.34	0.00	0.02	53.68	0.01	4.48
Record 3	12.00	0.00	26.48	1.78	3.14	100.26	57.69	81.87	22.13	5.57	0.02	0.31	0.00	22.30	0.97
Record 4	8.67	1.01	29.21	21.06	24.87	88.69	54.14	44.84	37.31	36.89	15.42	23.26		0.00	0.00
Record 5	7.77	0.64	18.68	21.91	14.89	52.68	60.72	22.36	30.80	50.57	0.00	9.28		1.83	3.34
Record 6	0.00	6.28	8.45	13.81	17.71	49.47	85.98	55.17	71.57	38.20				0.02	0.00
Record 7	0.00	2.95	3.98	14.25	0.90	69.44	75.57	75.75	72.06	44.82					1.10
Record 8	14.17	0.00	16.97	14.62	15.03	66.93	0.07	78.40	57.64	0.01					0.00
Record 9	5.57	0.40	0.00	0.00	9.35	33.69		81.75	59.83	8.03					1.66
Record 10	5.00	3.52	3.29	18.15	24.79	0.04		20.69	65.61	27.96					3.53
Record 11	6.14	3.39		32.39	13.09			25.84		36.46					
Record 12	1.52	5.21		25.42	16.84			25.45		36.46					
Record 13	0.48	0.16		27.85	26.23			0.01		61.34					
Record 14	7.12	4.09		28.61	24.92			12.71		60.85					
Record 15	1.51	0.00		16.31				0.00		51.72					
Record 16	1.59	3.09		15.70				0.00		76.51					
Record 17	0.00	0.00		22.12				4.70		78.77					
Record 18	7.83	0.00		13.64				17.90		65.17					
Record 19	6.33	0.75		20.67				24.68		49.45					
Record 20	10.06	12.24		29.94				20.49		49.45					
Maximum voltage (mV)															
Record 1	10.93	52.73	266.80	52.99	45.69	102.87	70.85	80.11	116.23	39.27	219.67	19.36	98.41	128.40	52.91
Record 2	9.81	21.46	22.95	4.89	0.47	99.85	42.24	82.60	30.74	28.94	722.00	112.63	70.40	407.56	7.72
Record 3	13.84	12.00	28.36	3.01	8.44	103.48	59.12	82.80	27.61	6.61	485.52	178.04	952.61	59.50	11.15
Record 4	12.28	3.51	31.39	24.88	28.98	96.82	58.33	57.64	38.58	39.47	350.78	65.84		600.43	2.96
Record 5	8.99	4.87	75.42	23.15	21.01	77.16	65.41	31.91	34.22	53.26	361.71	25.45		118.71	7.56
Record 6	3.17	7.27	12.12	14.86	25.77	74.55	266.76	80.50	91.66	42.18				128.61	8.71
Record 7	4.29	5.08	9.94	14.86	1.11	77.73	102.45	78.95	73.12	77.14					2.85
Record 8	25.22	2.63	20.15	18.49	16.85	69.20	71.41	84.31	57.91	11.12					0.88
Record 9	7.45	1.34	9.36	8.69	10.91	37.81		82.78	65.62	11.87					2.45
Record 10	8.38	14.61	3.81	28.73	26.73	113.62		28.34	65.91	33.35					8.70
Record 11	7.73	9.19		35.00	14.85			28.08		39.46					
Record 12	3.17	7.02		32.99	18.21			33.05		39.46					
Record 13	2.94	5.52		32.21	31.65			12.76		63.50					
Record 14	9.83	6.43		31.86	26.59			21.71		61.74					
Record 15	2.45	7.04		22.45				3.49		52.38					
Record 16	6.76	6.45		21.56				11.27		79.14					
Record 17	5.54	4.37		24.97				9.10		81.13					
Record 18	10.19	0.95		20.30				20.38		68.18					
Record 19	7.91	2.13		24.16				27.89		52.58					
Record 20	14.32	13.57		34.40				27.74		52.58					

Extended data Table 5. Isotope concentration values used for calculations of radiolytic O_2 production estimates.

Isotope	Seawater Concentration (ppb)	Reference	Nodule Concentration (ppm)	Reference
^{238}U	3	Choppin et al., 2002; Katz et al., 1986;	4	This study
^{235}U	0.022	Chen & Wasserburg, 1981	0.029	Chen & Wasserburg, 1981
^{232}Th	0.5	Choppin et al., 2002; Katz et al., 1986; Lide, 2004	11	This study
^{40}K	379	Draganic, 2005; Draganic et al., 1991	11900	Buchowiecki & Cherry, 1968; Nier, 1950

References for Extended Data Table 5

Choppin, G., Liljenzin, J-O., Rydberg, J. Radiochemistry and nuclear chemistry. Butterworth-Heinemann, (2002).

Katz, J.J., Seaborg, G.T., Morss, L.R. The chemistry of the actinide elements, second ed. Chapman and Hall, London New York, (1986).

Chen, J. H. & Wasserburg, G. J. Precise isotopic analysis of uranium in picomole and subpicomole quantities. *Anal. Chem.* **53.13,** 2060-2067 (1981).

Lide, D.R. ed. CRC handbook of chemistry and physics. **Vol. 85**. CRC press, (2004).

Draganić, I.G. Radiolysis of water: A look at its origin and occurrence in the nature. *Rad. Phys. Chem.* **vol. 72 (2–3)**, pp. 181–186 (2005).

Draganić, I.G. et al. Decomposition of ocean waters by potassium-40 radiation 3800 Ma ago as a source of oxygen and oxidizing species. *Precambrian Res.* **52(3–4)**, 337–345 (1991).

Buchowiecki, J. & Cherry, R.D. Thorium, radium and potassium in manganese nodules. *Chem. Geol.* **3 (2)**, 111–117 (1968).

Nier, A.O. A redetermination of the relative abundances of the isotopes of carbon, nitrogen, oxygen, argon, and potassium. *Phys. Rev.* **77 (6)**, 789–793 (1950).